Local ordering of nanostructured Pt probed by multiple-scattering XAFS

Agnieszka Witkowska*
Department of Solid State Physics, Gdansk University of Technology, 80-952 Gdansk, Poland

Andrea Di Cicco†
IMPMC-CNRS, Universitè Pierre et Marie Curie, 140 rue de Lourmel, 75015 Paris, France

Emiliano Principi
CNISM, CNR-INFM CRS SOFT, Department of Physics, University of Camerino, I-62032 Camerino, Macerata, Italy
(Received 25 May 2007; revised manuscript received 23 July 2007; published 20 September 2007)

We present detailed results of a multiple-scattering (MS) extended x-ray absorption fine structure (EXAFS) data analysis of crystalline and nanocrystalline platinum. Advanced MS EXAFS analysis has been applied to raw x-ray absorption data including the background, using the expansion of the absorption cross section in terms of local two-body and three-body configurations. Present EXAFS results on bulk Pt are found to be in agreement with previous structural and vibrational data, and has been used as a reference for reliable structural refinement of nanosized systems. EXAFS structural refinement of Pt nanoparticles has been performed in combination with electron microscopy and x-ray diffraction, showing the importance of considering the actual size distribution and morphology of the samples. Present samples were unsupported and supported Pt nanocrystalline systems with size distributions showing clusters of quasispherical shape in the 1–7 nm range. In particular, EXAFS spectra have been analyzed accounting for the reduction of the coordination number and degeneracy of three-body configurations, resulting from the measured size distribution and expected surface atom contributions. The importance of a correct account of the reduction of the number of neighbors for calculating MS contributions is emphasized in the paper. EXAFS results have been found compatible with x-ray diffraction and transmission electron microscopy investigations. We estimate that EXAFS could be used to study cluster shapes only for sizes below 2 nm using present methods and quality of the experimental data. We have also shown that the local distribution of distances and angles probed by EXAFS is broader than in bulk Pt, with first-neighbor bond length variance and asymmetry increasing upon reducing the particle size. Methods and results presented in this paper have been found to be successful for a robust structural refinement of monatomic nanocrystalline systems and represents a solid starting point for analyzing subtle structural and dynamical local changes occurring during *in situ* experiments involving nanomaterials for specific applications like supported nanocatalysts.

DOI: 10.1103/PhysRevB.76.104110 PACS number(s): 61.46.Hk, 61.10.Ht, 36.40.Mr, 82.45.Yz

I. INTRODUCTION

Understanding structure and dynamics of nanomaterials as well as their physicochemical properties is currently regarded as a challenging research activity having crucial consequences in material design for various novel applications. In this work, we focus our attention on the structural characterization of simple metallic nanomaterials as opposed to their bulk analogs using advanced x-ray absorption spectroscopy (XAS) data analysis.[1–4]

Metal nanoparticles of close-packing metals attract huge interest in applications, and they are now commonly used in our daily life. For example, supported metal nanoparticles of noble metals like Pt, due to their catalytic activity, are used in various applications, including fuel-cell technology. In spite of the relatively large diffusion of those materials, detailed *in situ* studies of their microscopic properties are still relatively rare. Typical materials to be studied are modest quantities (from micrograms to milligrams) of nanoparticles with typical size of 3 nm embedded in some matrix, so x-rays have been recognized as the most suitable probe for *in situ* microscopic studies. XAS, in particular, was used since the early times (see, for example, Ref. 5), and its application to the study of nanomaterials has been shown to provide useful complementary information[1,2,4,6] concerning the local atomic arrangement around the selected sites, their average electronic structure, and the subtle structural changes caused by various factors, e.g., method of preparation, working conditions, and aging.

Nowadays, very-high-quality data can be collected at modern synchrotron x-ray sources, even for very low photoabsorber surface density. Previous XAS investigations on a variety of free, supported, or embedded metal nanoparticles such as, e.g., Au, Ag, Pd, Co, Fe, and Pt, have been performed by several groups.[2–4,7–14] XAS spectra of close-packing systems contain important features associated with two- or three-body multiple-scattering (MS) signals. A great deal of information, including disorder, defects, and role and distribution of interface and surface atoms, is related to the details of the MS signals.[2] However, full MS data analysis probing higher-order correlations has been performed only in a few cases (see, e.g., Refs. 2–4 and 11).

In this paper, we face the problem of a robust structural refinement of metallic nanoparticles, using advanced MS analysis of extended x-ray absorption fine structure (EXAFS) data in combination with electron microscopy and x-ray diffraction, accounting for the actual size distribution and morphology. The importance of accounting for the size distribu-

tion of the nanocrystalline samples for XAS investigations was already emphasized, e.g., in Refs. 3, 4, 7, and 15.

We focus our attention on Pt nanoparticles used as catalysts, establishing a reliable framework for analyzing their structure in conditions relevant to actual fuel-cell operation. Up to now, *in situ* fuel-cell EXAFS measurements of nanometallic catalysts have been performed by various groups,[16–19] but the quality of the data was generally insufficient to realize detailed MS EXAFS analysis. Here, we present a robust methodology for MS EXAFS data-analysis of nanocrystalline close-packing fcc systems, applied to high-quality data collected *in situ*.[20]

The paper is organized as follows: Section II is dedicated to a presentation of the experimental details; this means sample and experimental setup description (Sec. II A) and detailed morphological and particle size distribution characterization (Sec. II B). Section III is focused on the methodology of the XAS data analysis using an advanced technique based on the GNXAS method[21,22] in application to Pt samples; results of the MS data analysis of Pt foil and samples with Pt nanoparticles are shown and discussed in Sec. IV. In Sec. V, the main conclusions of this work are given.

II. EXPERIMENTAL DETAILS

A. Sample description and x-ray absorption measurements

Accurate XAS experiments were performed on samples of nanocrystalline Pt and on a 5 μm Pt foil, taken as reference for a bulklike material in the successive data analysis.

The samples of nanocrystalline Pt were obtained using commercially available products, normally used as catalyst materials in fuel-cell applications. In particular, two different products were chosen, showing different characteristics: the first, C-6, was a commercial nanocatalyst with typical crystallite sizes of the order of 6 nm (C-6, unsupported HP Platinum Black from E-TEK Division); the second, EL-20, was an electrode for fuel cells (EL-20-10-10 from Quintech, Pt loading: 1.0 mg/cm^2) with typical crystallite sizes in the 3 nm range. Three different samples for XAS absorption measurements were, thus, produced using those products, hereafter called Pt1, Pt2, and Pt3, respectively: (1) sample Pt1 was obtained by carefully mixing the C-6 powders and graphite, producing a pellet with average Pt thickness chosen to give an optimal jump at the absorption edge ($J \sim 0.8$); (2) sample Pt2 was simply the ready-to-use EL-20 electrode, where the absorption jump at the Pt L_3 is not optimized and possible thickness inhomogeneity can occur; and (3) sample Pt3 was a working membrane electrode assembly (MEA) installed inside a fuel cell especially optimized for XAS measurements (for details, see Ref. 20). MEA was composed of the Pt2 electrode as a cathode catalyst (oxygen reduction side), Nafion N-117® as a proton conductive membrane, and Pd-based electrode (30% Pd/Vulcan XC-72 powder, with Pd loading of 1.0 mg/cm^2) as an anode catalyst (hydrogen oxidation side). The MEA worked at 0.805 V vs the reversible hydrogen electrode (RHE) at ambient temperature, while gas flow (oxygen and hydrogen) was set to about 100 ml/min.

This set of samples was chosen in order to study the role of nanocrystallite size distribution, homogeneity, and the effect of the x-ray absorbing cell environment in nanocatalyst materials and components relevant to fuel-cell applications. High-quality Pt L_3-edge XAS spectra were recorded at the Synchrotron Light Laboratory ELETTRA (XAFS station, Trieste, Italy) and at the European Synchrotron Radiation Facility (BM29, Grenoble, France) using double-crystal monochromators equipped with Si(111) and Si(311) crystals, respectively. XAS measurements presented here were performed in the 11.40–13.1 keV energy range (the Pt L_3-edge energy is at 11.564 keV) under ambient conditions.

B. Nanocrystalline sample characterization

Information about the average size of nanocrystallites used in this work can be found in the data sheet of the producers. However, proper detailed sample characterization is needed to perform a careful and reliable XAS data analysis (see next sections), with the final aim of detecting and studying the details of the local structure in these ill-ordered systems. In particular, detailed morphological investigations should be performed prior to any XAS analysis in order to study crystallite size distribution, their shape, and homogeneous distribution through the sample. Therefore, we have used transmission electron microscopy (TEM), x-ray diffraction (XRD), and scanning electron microscopy (SEM) measurements to obtain various essential mesoscopic and nanoscopic information about the samples.

TEM-image analysis (200 randomly selected quasispherically shaped particles) of samples Pt1 and Pt2 (Pt3) was carried out to study the actual nanoparticle size distributions (TEM Philips CM-10). A typical image of scraped material from sample Pt2 (Pt3) shows nanoparticles of nearly spherical shape as shown in the upper part of Fig. 1. The same, nearly spherical, shape has been obtained for the Pt1 sample. However, in this case, it was very difficult to obtain TEM images suitable for crystallite size analysis due to the presence of aggregates.

The size distributions of samples Pt1 and Pt2 (Pt3) are shown in the lower part of Fig. 1. The distributions are asymmetric and show a tail extended to large-sized nanoparticles. The Pt1 and Pt2 (Pt3) size distributions are reproduced rather accurately through a lognormal model.[23] In the first case (Pt1), the mean particle diameter of the lognormal distribution is found to be $D=4.32\pm0.06$ nm with standard deviation $\sigma=0.8\pm0.1$ nm. For the second sample (Pt2 and Pt3), instead, we obtain $D=2.56\pm0.05$ nm and $\sigma=0.9\pm0.1$ nm (see also Table I). We note, however, that very small particles (diameters less than 1 nm) could not be detected, while the weight of larger particles could be slightly underestimated, due to the opacity of thicker sample regions. In any case, the two samples Pt1 and Pt2 were clearly characterized to have different well-defined size distributions.

The Pt crystallite sizes have also been estimated by analyzing x-ray diffraction patterns (details on the x-ray diffraction setup can be found in Ref. 24) through the Scherrer equation.[25,26] We considered the shape of the (111), (200), (220), (311), and (222) peaks, as shown in Fig. 2 and Table I. Line profiles have been modeled with a Voigt function, using a Gaussian component to correct for instrument contribution

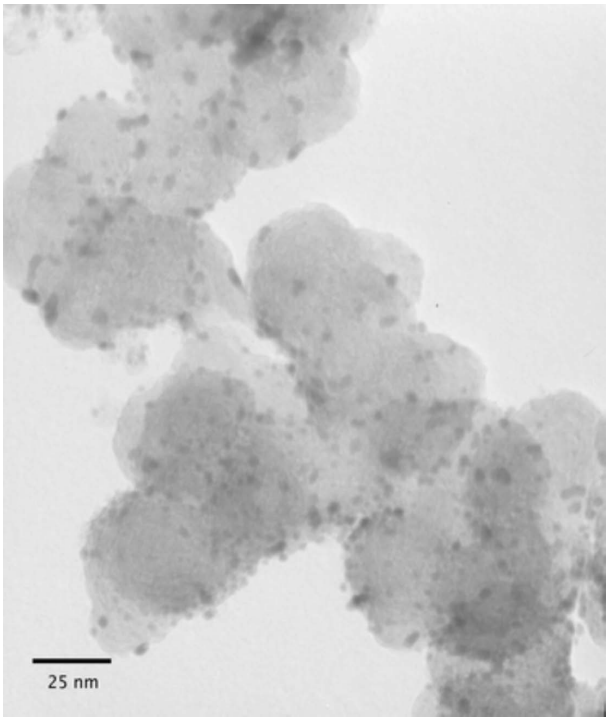

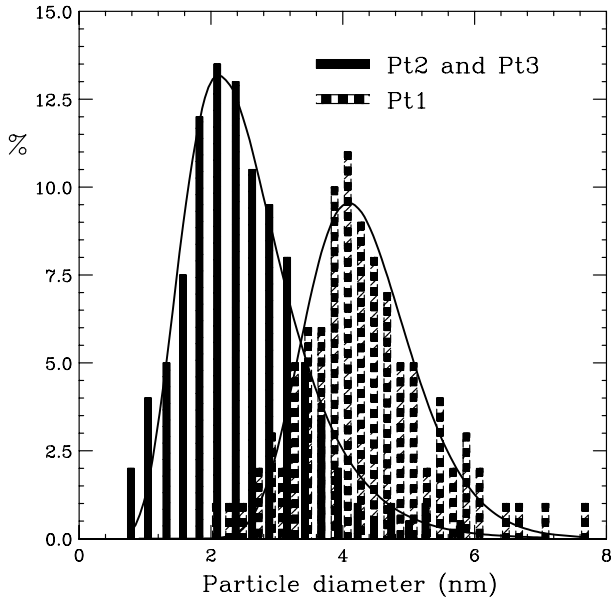

FIG. 1. (Top) TEM image of the Pt catalytic material scraped from the electrode (Pt2 and Pt3) and (bottom) comparison between nanoparticle size distributions obtained for Pt2/Pt3 and for Pt1.

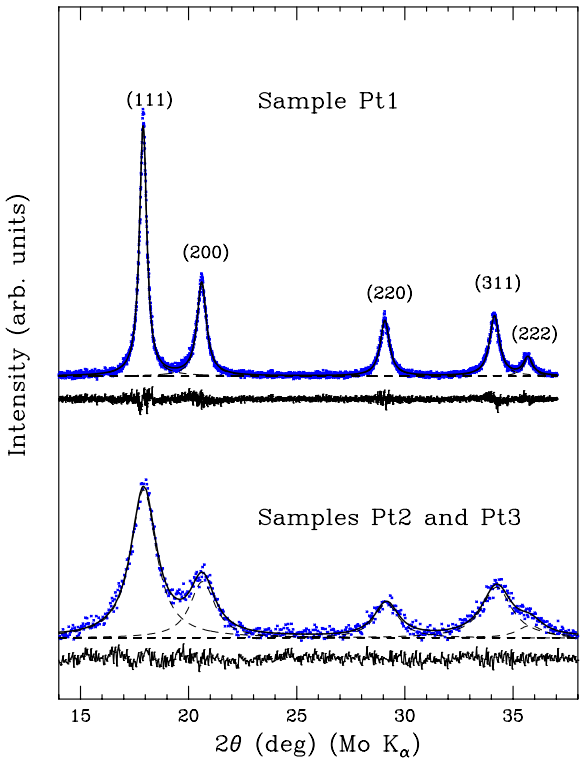

FIG. 2. (Color online) X-ray powder diffraction patterns of the nanocatalysts under consideration (Pt1, Pt2, and Pt3). Experimental data (points, blue) are compared with the calculations using Voigt functions (solid and dashed lines). The agreement with calculated spectra is excellent, and the residual curves are shown below each diffraction pattern.

to peak broadening ($\sigma_{corr}=0.1°$) (program PEAKFIT, see, e.g., Refs. 27 and 28). We accounted for relatively narrow particle size distributions (Scherrer constant $K=0.9$), obtaining reasonable average diameter values for each Bragg peak under consideration. The average size of Pt nanoparticles as obtained by averaging the results of the data analysis of the five Bragg peaks, were determined to be 7.4±0.4 and 2.7±0.2 nm for Pt1 and Pt2 (Pt3), respectively, as shown in Table I.

Data presented in Table I show that average sizes estimated using TEM and XRD are in excellent agreement for Pt2 (Pt3), while XRD values are slightly overestimated for the Pt1 sample. This is consistent with observations reported in Ref. 14, where XRD mean sizes were found to be weighted more toward larger crystallites. In the Pt1 sample, the tail of the distribution extends to distances larger than

TABLE I. The diameter of platinum nanocrystals (in nm) estimated from XRD line profile analysis (peak position and full width at half maximum intensity) using the Scherrer equation with the Scherrer constant $K=0.9$. The last column contains average sizes obtained by analyzing TEM images.

Sample	Peak (111)	Peak (200)	Peak (220)	Peak (311)	Peak (222)	XRD d_{ave} (nm)	TEM D (nm)
Pt1	7.7	7.1	7.4	7.0	7.6	7.4	4.32
Pt2	2.6	2.7	2.8	2.5	2.9	2.7	2.56

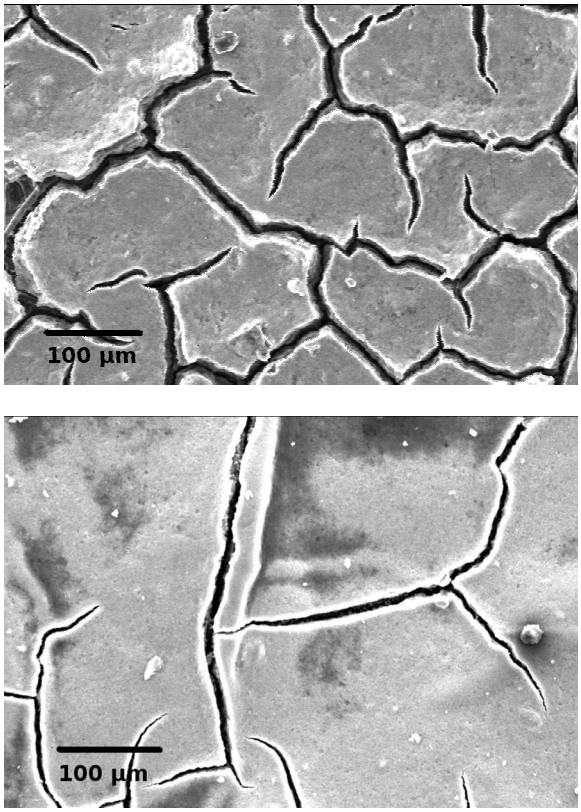

FIG. 3. SEM images of the Pt electrode surfaces: (top) $a \approx 0.1$ and (bottom) $a \approx 0.04$.

6–8 nm and the presence of a few large particles in the ~10 nm range is able to shift the measured mean value significantly.

Another important problem for XAS measurements is the sample homogeneity. The importance of using homogeneous samples of suitable average thickness for XAS measurements of nanocrystalline materials was widely emphasized, for example, in Refs. 3 and 29. In the spirit of performing *in situ* measurements of catalysts during their actual cycles, it is necessary to verify possible inhomogeneity of the electrode surfaces. To this purpose, SEM analysis has been used for the characterization of the morphology of the samples. In Fig. 3, we show images of electrodes used in the fuel cell. The top image shows an electrode where there are severe problems of homogeneity of distribution of Pt nanocrystallites: many holes and cracks are observed, and we estimate that about 10% of the sample surface is completely free from catalytic material ($a = S_{holes}/S_{tot} \approx 0.1$). The lower image represents the commercial electrode used in this work (Pt2 and Pt3 samples), which appears to be more homogeneous ($a \approx 0.04$).

The consequences of an inhomogeneous distribution of photoabsorbing atoms in transmission XAS experiments are quite well known.[30,31] In the presence of a thickness distribution, nonlinear effects are found to reduce the contrast in the spectra. In particular, it has been shown that the experimental absorption signal $\alpha(E)$ can be expressed using a cumulant expansion[32] in terms of the sample thickness distribution, and the effect of holes on well-defined fractions of the sample surface can be easily verified.

The situation observed in our electrodes can be roughly represented through a steplike thickness distribution:

$$P(l) = a\,\delta(l) + (1-a)\,\delta(l-l_0), \tag{1}$$

for which the absorption coefficient takes the following form:

$$\alpha = \mu l_0 - \left[a(e^{\mu l_0} - 1) - \frac{a^2}{2}(e^{\mu l_0} - 1)^2 + \cdots \right], \tag{2}$$

where $\delta(l)$ is the Dirac δ function, a is the fraction of sample surface with holes ($a = S_{holes}/S_{tot}$), and μl_0 is the ideal absorption coefficient for a homogeneous layer of thickness l_0. We have verified that corrections are needed for a value of a greater than 0.1 (see, for example, the sample surface presented in the top image of Fig. 3); however, for electrodes used in this work ($a \approx 0.04$), the amplitude correction is well below 1%, so samples can be considered homogeneous for XAS data-analysis purposes.

III. X-RAY ABSORPTION SPECTROSCOPY DATA ANALYSIS: METHODOLOGY AND APPLICATION TO Pt SAMPLES

A. Data-analysis method

Modern XAS data analysis provides a structural refinement of the raw XAS data through MS calculations of the x-ray absorption cross section. In particular, the GNXAS data-analysis method for XAS data analysis is designed to produce fast and accurate simulations of the $\gamma^{(n)}$ MS XAS n-body signals, associated with the n-body distribution functions, g_n, describing the local structure around selected photoabsorbing atoms.[21,22] The standard XAS structural refinement is based on modeling the short-range distribution functions as a sum of distinct peaks associated with well-defined bonding distances and angles corresponding to first and farther neighbors for the pair (g_2) and higher-order (g_n, $n>2$) distribution functions.[22,33] The basic expression for the XAS structural signal $\chi(k)$ is

$$\begin{aligned} \langle \chi(k) \rangle = & \int_0^\infty dr\, 4\pi\rho r^2 g_2(r)\, \gamma^{(2)}(r,k) \\ & + \int dr_1 dr_2 d\theta\, 8\pi^2 r_1^2 r_2^2 (\sin\theta)\rho^2 \\ & \times g_3(r_1, r_2, \theta)\, \gamma^{(3)}(r_1, r_2, \theta, k) + \cdots, \end{aligned} \tag{3}$$

which turns out to be a sum of regular oscillations as a function of the photoelectron wave vector k. The integral is short ranged because of the rapid amplitude decay of the $\gamma^{(n)}$ functions at large distances. The peak-fitting approach is widely justified for molecules and in ordered condensed matter, where the assumption about the existence of distinct g_2 and g_3 peaks at short distances is fulfilled and well-defined bond distances and angles can be easily defined. In these systems, such a scheme represents a fast and efficient tool, usually able to guarantee a reliable reconstruction of the shape of the short-range distributions through a limited number of structural parameters. However, owing to the short-range sensi-

tivity of the XAS phenomenon, the definition of suitable model functions is particularly important. Gaussian shapes work fine whenever the harmonic approximation for vibrations holds, but deviations have been observed and studied even at moderate temperatures. Non-Gaussian model functions have been devised and have been successfully used in a variety of cases[21,22,28,34–38] for solid and liquid systems. In particular, a simple asymmetric Γ function model[39] including a skewness parameter β has been found to be particularly useful for reproducing the shape of the first-neighbor distribution in most solid and liquid systems.[28,35–37,39] The shape of the first-neighbor distribution can then be safely reconstructed, overcoming the severe limitations of the cumulant expansion technique (see Ref. 28, and references therein).

The application of this data-analysis method is especially important for understanding the subtle structural modifications occurring in nanostructured materials, which are, of course, ill-ordered materials. When the number of surface atoms becomes important, we expect substantial modifications in the shape of the g_n distributions for any order n. In particular, the peaks of the g_2 (and g_3) distribution will be modified according to their area (degeneracy and coordination number), shape (variance and skewness), and mean value (average distance R). In previous papers, the GNXAS method was applied to various nanocrystalline systems showing the importance of accounting for induced defects in those obtained by high-energy ball milling,[2] and the role of multiple scattering in those and other nanophase[3] systems. The importance of accounting for multiple scattering in XAS data of Pt nanoparticles was also discussed in Refs. 4 and 40 using a more popular data-analysis approach [FEFF (Ref. 41)]. Moreover, the need of a sample with homogeneous thickness distribution (as discussed in Sec. II B) was widely emphasized in Refs. 3 and 29 for a reliable evaluation of the reduction in coordination number due to the increased surface-to-volume ratio.

The samples under consideration, as shown in Sec. II B, are homogeneous ensembles of Pt nanocrystalline particles acting as a catalyst on the electrodes, and their average local structure is obviously very similar to that of bulk crystalline Pt. The variation of the XAS signal in nanocrystalline Pt as compared to the bulk can be used to infer information about the corresponding changes in the local structure and dynamics, provided that a good modeling of bulk local properties is obtained. For this reason, we performed an accurate modeling of bulk Pt using GNXAS, obtaining background and nonstructural parameters to be used for a meaningful comparison with the corresponding nanocrystalline systems. Present Pt L_3-edge XAS experimental data have, thus, been analyzed using MS contributions through n-body γ signals in the XAS data analysis.[21,22] The two-body and three-body [$\gamma^{(2)}$ and $\gamma^{(3)}$] signals have been calculated starting from the model fcc structure using nonoverlapping potentials within the muffin-tin approximation ($R_{MT}=1.18$ Å for a first-neighbor (FN) distance, $R_{FN}\approx 2.77$ Å). Phase shifts have been calculated using various forms for the exchange-correlation potentials. Dirac-Hara and Hedin-Lundqvist energy-dependent potentials, both real and complex, have been tested. For complex potentials, the inelastic mean free path (MFP) of the excited photoelectron, $\lambda(E)$, has been calculated automatically and the core hole lifetime has been defined as a constant parameter taken from Ref. 42. For real potentials, the MFP curve was modeled using the following expressions:

$$\lambda = Ak^{\delta} + \frac{B}{k^4}, \tag{4}$$

with three parameters A, B, and δ, which can be chosen in such a way as to reproduce accurately the MFP tabulated in Ref. 43, where measured and calculated data are included. The best-fit result for bulk Pt, presented below, has been obtained using real Hedin-Lundqvist exchange potential with $A=0.7$ Å$^{2.1}$, $B=1000$ Å^{-3}, and $\delta=1.1$.

The XAS signal, as defined by Eq. (3), has been calculated for various two-body and three-body configurations described in Table II. Due to the limited electron MFP and atomic vibrations, at room temperature, the main frequency components contributing to the measured $\chi(k)$ signal are limited within a sphere of about 6 Å around the photoabsorbing atoms.

The $\gamma^{(2)}$ and $\gamma^{(3)}$ signals have been averaged using asymmetric Γ functions for the two first g_2 peaks, and Gaussian models for further g_2 and g_3 peaks. The structural refinement has been performed by minimizing the difference of the raw absorption from the model data computed by multiplying the structural oscillation, $\chi(k)$, by a suitable background normalizing factor, which is a standard practice with GNXAS.[22] It is important to remark that the chosen atomic background includes contribution of many-electron channels, amounting usually up to a few percent of the absorption cross section. As widely discussed elsewhere, inaccurate modeling of the atomic background can result in the presence of low-frequency components without structural origin in the XAS

TABLE II. Two-atom (g_2) and three-atom (g_3) configurations in a typical fcc structure: R_1 is the mean distance between atoms (g_2); R_1, R_2 are the mean distances of two shortest bonds with angle Θ in between; R_3 is a mean distance of the longest bond (g_3); and R_0 is the first-neighbor distance. Degeneracy is specified for each configuration, with the photoabsorber placed at the vertex between two shortest bonds.

	R_1/R_0	R_2/R_0	Θ (deg)	Degeneracy	R_3/R_0
$g_2^{(1)}$	1			12	
$g_2^{(2)}$	$\sqrt{2}$			6	
$g_2^{(3)}$	$\sqrt{3}$			24	
$g_2^{(4)}$	2			12	
$g_2^{(5)}$	$\sqrt{5}$			24	
$g_3^{(1)}$	1	1	60	24	1
$g_3^{(2)}$	1	1	90	12	$\sqrt{2}$
$g_3^{(3)}$	1	1	120	24	$\sqrt{3}$
$g_3^{(4)}$	1	1	180	6	2
$g_3^{(5)}$	1	$\sqrt{2}$	90	24	$\sqrt{3}$
$g_3^{(6)}$	1	$\sqrt{3}$	73.22	48	$\sqrt{3}$
$g_3^{(7)}$	1	$\sqrt{2}$	135	24	$\sqrt{5}$

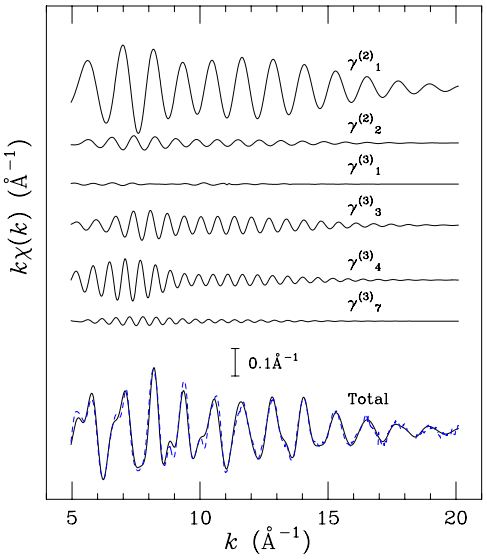

FIG. 4. (Color online) The best-fit results of GNXAS analysis performed for Pt foil at Pt L_3 edge (k^3 weighted). Upper curves represent components of the model signal, vertically shifted for clarity: solid line, model signal; dashed blue line, experimental signal. The scale is indicated within the figure (0.1 Å^{-1}).

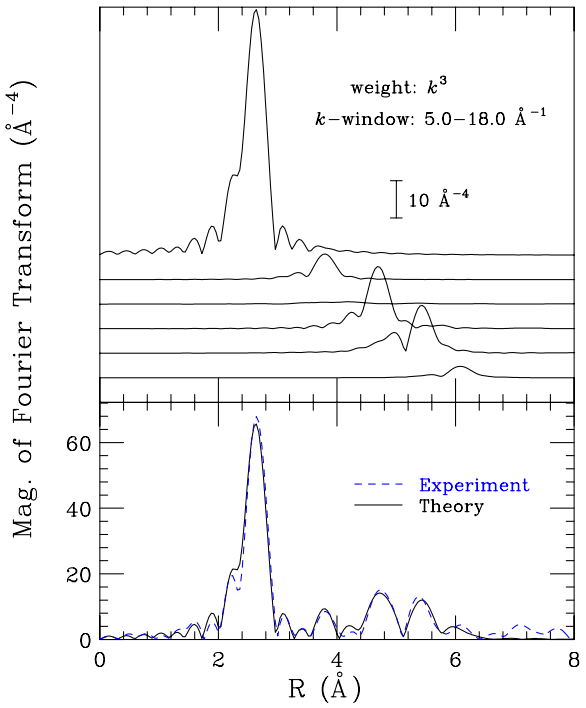

FIG. 5. (Color online) Magnitude of the Fourier transforms calculated with a k^3 weight in the range of k=[5.0;18.0] Å^{-1}. (Top) The successive contributions vertically shifted for clarity (see also Fig. 4); the scale is indicated within the figure (10 Å^{-4}). (Bottom) The comparison between total theoretical signals and experimental one.

structural signal. In this study, we have used the same background shape for our Pt samples by including the contribution of specific double-electron excitation channels ($2p\,4f$) and ($2p\,4p$) (about 110–130 and 500 eV after the absorption edge, respectively), in agreement with previous studies.[44,45]

B. Application to crystalline Pt

In the case of crystalline platinum (fcc structure), the main frequency content of the EXAFS signals (confined within 5–6 Å) are presented in Table II. In order to avoid parameter proliferation in a fitting procedure, it is necessary to group as many signals as possible provided that they originated from the same atom configuration. In some previous works, a single distance parameter was used to define all of the MS signals contributing to the EXAFS spectra, keeping fixed coordination numbers (see, for example, Refs. 2 and 46). In the present case, we used first- and second-neighbor interatomic distances to define both two- and three-body contributions in our simulated EXAFS signals, still keeping fixed bond angles and coordination numbers. In particular, the first five shells and four three-body configurations have been used to fit experimental spectra. The following structural contribution and associated parameters have been considered (refer also to Figs. 4 and 5, upper curves):

(1) The first-shell total two-body signal, $\gamma^{(2)}{}_1$, modeled as a Γ distribution with four parameters: average distance R_1, variance σ_1^2, and skewness β_1 of the bond-length distribution and coordination number N_1 (fixed to 12).

(2) The second-shell total two-body signal, $\gamma^{(2)}{}_2$, treated as in (1), with parameters R_2, σ_2^2, β_2, and $N_2=N_1/2$.

(3) The first equilateral three-body configuration (triangle degeneracy 8.0), in which all of the atoms are equivalent and there is a single $\gamma^{(3)}{}_1$ signal with degeneracy 24. The geometry is defined by an angle of 60° (fixed) and previously introduced parameters R_1 and σ_1^2. The correct account of this triplet configuration requires only the addition of a single structural parameter of the covariance matrix, correlated variance between the vibration of the first-neighbor bonds, $\rho_{r,r'}$.

(4) The next contribution related to a triangle with two first-neighbor bonds and vertex angle of 120°. It should be noted that the long bond of the triangle corresponds to the third shell of the fcc structure. Therefore, the fourth signal presented in Fig. 4, $\gamma^{(3)}{}_3$, is associated with $g_2^{(3)}$ and $g_3^{(3)}$ configurations (see Table II). The equilibrium position of this triangle is defined by R_1, $N_3=2N_1$, $\Theta=120°$ (fixed), and covariance matrix parameters: σ_1^2, $\sigma_{\Theta_{120}}^2$, $\rho_{r,r''}$, and $\rho_{r,\Theta_{120}}$ (only three new ones).

(5) Collinear three-body configuration, $\gamma^{(3)}{}_4$ (an important and strong contribution). In this case, a long bond signal corresponds to the fourth coordination shell. The signal represents $g_2^{(4)}$ and $g_3^{(4)}$ configurations, as indicated in Table II. This contribution requires only two new fitting parameters: $\sigma_{\Theta_{180}}^2$ and $\rho_{r,r'''}$. Coordination number N_4 is equal to N_1.

(6) The fifth-shell contribution derived from the triangle configuration with one first-neighbor and one second-neighbor bonds and vertex angle of 135°, the last signal shown in Fig. 4, $\gamma^{(3)}{}_7$. In this case, three new fitting parameters appear (angle is fixed): $\sigma_{\Theta_{135}}^2$, $\rho_{r,r'v}$, and $\rho_{r,\Theta_{135}}$.

Comparison in the energy space between the experimental signal and theoretical one has been performed without any

pretreatment of the data, optimizing the structural and some nonstructural parameters. The fitting was performed using 15 structural parameters measuring the average structure and correlated dynamics. Other 12 nonstructural parameters correspond to E_0 (edge energy, defined as the difference between experimental and theoretical energy scales), S_0^2 (amplitude of the one-electron channel), experimental resolution, three MFP curve parameters, and two three-parameter double-electron excitation arctangentlike model functions[33] (see Sec. III A). The quality of the fitting can be appreciated by looking at Figs. 4 and 5 (lower panels), where experimental and calculated spectra and their Fourier transforms are compared. A detailed discussion of the results is reported in Sec. IV.

C. Application to Pt nanoparticles

XRD and XAS data of samples Pt1, Pt2, and Pt3 show that the nanoparticles have an inner fcc structure, although limited in size. Clearly, MS data analysis can be largely based on that of bulk Pt exposed in Secs. III A and III B, taking proper account of the particle size.

As shown in Sec. II B, samples of nanocrystalline Pt (Pt1–Pt3) have been fully characterized by XRD, SEM, and TEM, ruling out possible artifacts due to the inhomogeneity of the samples and determining the size distribution and the average size of the particles.

The nanometric size of the particles clearly affect the multiplicities of the typical MS signals associated with the two-body and three-body configurations of the fcc structure (see g_2 and g_3 peaks in Table II). Of course, the presence of surface "ill-coordinated" atoms, depending on size and shape of the grains, affects both the degeneracy associated with two-body and three-body peaks and disorder-related quantities such as variances of distances and angles, and asymmetry. All these effects are deeply correlated; therefore, an independent evaluation of the size distribution of the particles and of the expected degeneracy of the various two- and three-body configurations is extremely useful for a robust EXAFS data-analysis.

For these reasons, we have calculated the multiplicities of the main local two-body and three-body fcc configurations as a function of the grain size using cuboctahedral models for quasispherical and hemispherical [truncated along (111), (110), and (100) planes] clusters, possibly models for the nanoparticle shape of unsupported and supported Pt. Results for quasispherical and (111)-truncated clusters are shown in Fig. 6. Results for hemispherical particles truncated along the other planes have been found to be very similar to the (111)-truncated cluster shown in Fig. 6.

Looking at Fig. 6, we see that even for relatively small clusters, with sizes in the 2–5 nm range, it is very important to account for the changes in coordination numbers or degeneracy of distant shells and of three-body configurations.[2–4] The three-body configurations are mainly the collinear ones at 180° (associated with the strongest EXAFS signal) and also configurations with angles of 120° and 135°, showing pronounced degeneracy changes. Thus, Fig. 6 is a simple demonstration of how accounting for MS signals is so important in the EXAFS data analysis of the nanoscale systems.

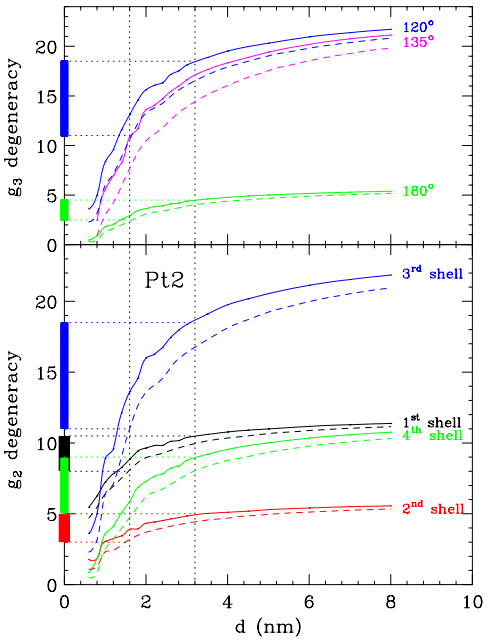

FIG. 6. (Color online) Two- and three-atom configuration degeneracies (photoabsorber placed at the vertex between two shortest bonds) as a function of particle diameter, calculated using a model of quasispherical Pt clusters (solid lines) and hemispherical (111)-truncated Pt clusters (dashed lines). The variation ranges for degeneracy values (bands shown on the y axis) used in the case of Pt2 sample are also presented. Two vertical dotted lines define Pt2 nanoparticle size limits resulting from TEM/XRD analysis (see Fig. 1 and Table I).

TEM and XRD analyses of the particle size distribution and shape reported in Table I provide us useful constraints on the degeneracy of the two-body and three-body configurations to be used for the EXAFS fitting of samples Pt1–Pt3 containing nanoparticles. Constraints are associated with the measured size distribution, and an example (for sample Pt2) is reported in Fig. 6 (each band is related to a specified n-atom configuration degeneracy). However, it should be noted that for supported Pt nanoparticles (Pt2 and Pt3) which could be characterized by quasispherical and/or hemispherical shapes,[4,12] we used limits accounting for both possible morphologies, while for the Pt1 sample, composed of unsupported Pt nanoparticles, we assumed that they have quasispherical shape.

Finally, to the purpose of EXAFS refinements of Pt nanoparticles, we have used the same decomposition and techniques for calculation of the MS signals described in Sec. III B, taking into account some important constraints:

(1) degeneracy of the MS signals has been floated within a range obtained by the measured size distribution of the nanoparticles;

(2) the presence of surface ill-coordinated atoms in nanosized systems affects also the bond distance and bond-angle distributions, and values of distance and angle variances of bulk Pt (foil) have been taken as lower limits of the corresponding distributions;

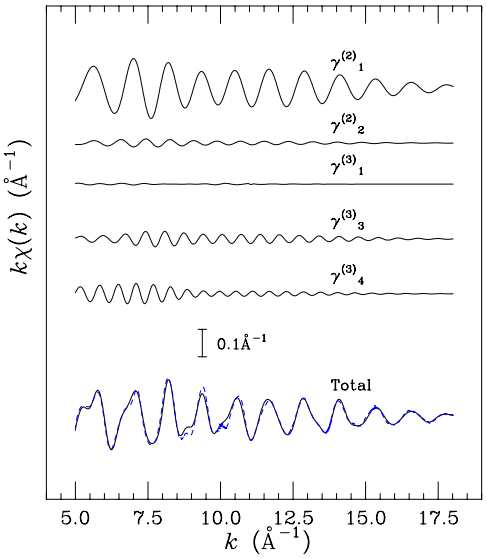

FIG. 7. (Color online) The best-fit results of GNXAS analysis performed for Pt1 sample at Pt L_3 edge (k^3 weighted). Upper curves represent components of the model signal: solid line, model signal; dashed blue line, experimental signal. The scale is indicated within the figure (0.1 Å^{-1}).

(3) background model was the same as used in bulk crystalline Pt (foil), while other nonstructural parameters were fixed to the values obtained for bulk Pt within their estimated uncertainty (S_0^2,E_0).

These constraints have been found to guarantee a robust structural refinement of these nanocrystalline Pt samples, using a total of 16 structural parameters. These are the same as those for bulk Pt, excluding three of those associated with the fifth shell (sixth in the list of Sec. III B) which are found to give a negligible signal, and including four multiplicity parameters of the relevant two-body and three-body configurations floated in the restricted ranges specified above.

The quality of the GNXAS analysis obtained for the Pt1 sample and the type of individual MS signals used for refining EXAFS data of Pt nanoparticles are shown in Fig. 7. The changes in intensity of the individual and of the total EXAFS signals can be appreciated by looking at Fig. 4, where we report those of bulk Pt. Detailed results of GNXAS multiple-scattering structural refinements are presented in the subsequent section.

IV. RESULTS AND DISCUSSION

Detailed best-fit results and structural parameters obtained for each Pt sample by using GNXAS MS method are presented in Figs. 8 and 9 and Tables III and IV.

First, let us discuss briefly the results obtained for Pt foil which will serve as a reference for further analysis and discussion of the nanocrystalline Pt samples Pt1, Pt2, and Pt3. As it is shown in Figs. 4 and 5, the MS best-fit calculations provide an accurate fitting of the experimental data by considering two-body and three-body contributions up to the fifth coordination shell. The parameters defining the first-

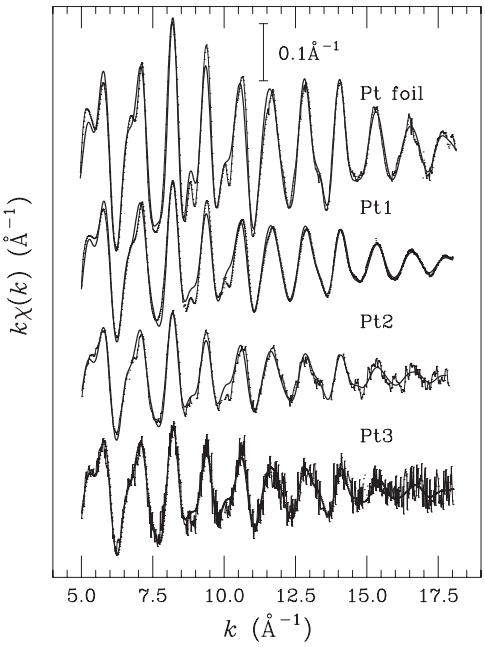

FIG. 8. Comparison between experimental $k\chi(k)$ spectra and the best-fit calculated signals obtained using multiple-scattering contributions for each sample. The scale is indicated within the figure (0.1 Å^{-1}).

shell distribution (i.e., R, σ^2, and β for shell I in Table III) are those measured with higher accuracy as they are related both to the direct first-neighbor two-body signal and to several MS contributions.

Best-fit first-neighbor results are in good agreement with crystallographic and vibrational data found in the literature (see, e.g., Refs. 4, 10, 45, 47, and 48). In particular, the bond variance σ^2 is in good agreement with previous calculations[47] (cf. 0.0049 Å^2). The same holds for the second

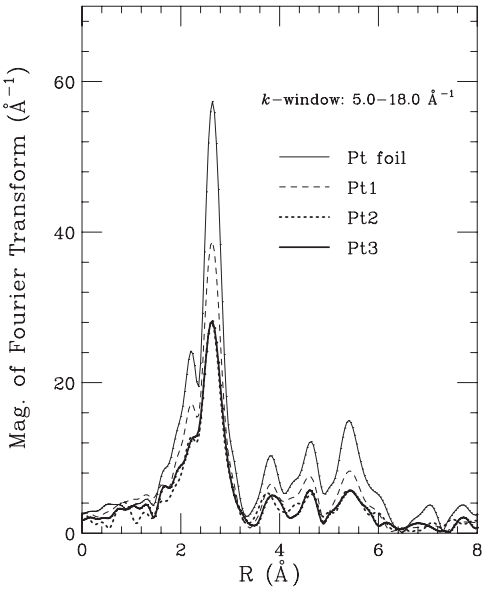

FIG. 9. Fourier transforms of total $\chi(k)$ signals calculated for the experimental EXAFS data presented in Fig. 8.

TABLE III. Structural parameters of the two-body configurations obtained by GNXAS analysis for each sample, where R (Å) is the average interatomic distance, σ^2 (10^{-3} Å^2) is the distance variance, β is the skewness parameter, N is the coordination number, and f is a fixed value.

	Pt foil				Pt1				Pt2				Pt3			
Shell	R	σ^2	β	N	R	σ^2	β	N	R	σ^2	β	N	R	σ^2	β	N
I	2.766(2)	4.9(1)	0.00(5)	12.0_f	2.761(2)	5.8(1)	0.06(5)	11.3(5)	2.768(5)	6.9(5)	0.2(1)	9.6(8)	2.77(1)	7(1)	0.2(2)	9.3(1.0)
II	3.909(5)	7.4(8)	0.00(5)	6.0_f	3.903(5)	8.3(8)	0.00(5)	5.2(5)	3.91(1)	8(2)	0.1(2)	4.5(8)	3.91(2)	9(4)	0.1(5)	4.4(1.5)
III[a]	4.790(4)	7(3)	0.0_f	24.0_f	4.782(4)	8(4)	0.0_f	21(2)	4.79(1)	8(5)	0.0_f	16(3)	4.79(2)	8(7)	0.0_f	15(6)
IV[a]	5.528(4)	9(3)	0.0_f	12.0_f	5.518(4)	10(4)	0.0_f	11(1)	5.53(1)	10(5)	0.0_f	8(2)	5.52(2)	10(7)	0.0_f	8(3)

[a]Parameter derived from the three-atom configuration.

(0.0070 Å^2 from Ref. 47) and farther shells, for which the distance variance is found to approach the uncorrelated limit $2\langle u^2\rangle$ ($\langle u^2\rangle$ is the fluctuation around equilibrium positions). Possible deviations from the Gaussian approximation have been investigated by using Γ distribution. The present result, $\beta \approx 0.0$, indicates that for crystalline Pt, the harmonic approximation holds at room temperature. As described in Sec. III B, MS contributions related to third, fourth, and fifth neighbors allow us to measure bond-angle variances and bond-bond and bond-angle correlations for those three-body configurations. Major parameters defining the three-body distribution for three-body configurations are reported in Table IV. Those parameters have been used to calculate the resulting bond variances of the third and fourth shells (see Table III), as usual when higher shells are considered through three-body configurations.[2,22] First-neighbor bond-bond correlations $\rho_{r,r'}$ have been found to be negative, in agreement with previous results, indicating a slight anticorrelation in the vibration along the bond directions. The uncertainty on the other covariance matrix parameters[22,33] (not shown in Table IV) defining the three-body distributions is very large, as their variation has negligible effects on the calculated MS signal.

On the basis of the results obtained for bulk Pt, we can now proceed in discussing the EXAFS results for our nanocrystalline samples. The quality of the measured EXAFS signals even in the case of very low Pt loading is extremely good, as shown in Fig. 8. This gives us the possibility to observe changes in the features related to high-frequency components, as shown also by the Fourier transforms (FTs), where we can identify and consider all of the peaks up to a distance of 6 Å (farther peaks are related to higher shells and triangular configurations, see Sec. III A and Figs. 4 and 5). The main change is a reduction of the $\chi(k)$ signal amplitude and of the intensity of the FT peaks in nanocrystalline materials. This is mainly caused by a decrease in the average coordination numbers (degeneracy). However, it is interesting to note that there is a more pronounced reduction of the FT peaks than is expected by the size of the nanocrystallites, and additionally, this damping increases for peaks located at higher distances (refer to Fig. 9). For example, the height reduction for the first-neighbor peak is about 35% and 50% for Pt1 and Pt2 (Pt3), respectively, while the expected reduction due to the decrease in the average coordination number is only 12% for Pt1 and about 20% for Pt2 (Pt3). However, this is easily explained by a corresponding increase in the structural disorder (see results of EXAFS analysis in Tables III and IV), which also affects the amplitude of the signals and of the FT peaks, as is well known. Increase of structural disorder and reduction of coordination numbers are strongly correlated quantities, but act differently on the MS signals due to their different k dependence, so their decoupling is possible by fitting the raw data without Fourier filtering.

Refinement of EXAFS signals of the Pt1–Pt3 samples provided accurate measurements of the first- and second-neighbor distributions, while uncertainties on the farther shells were found to be larger (see Table III). Uncertainties affecting the structural parameters were evaluated using standard statistical procedures for multiparametric fitting of raw data, as discussed, for example, in Refs. 22 and 33. Error bars on structural parameters depend on the noise level and energy extension of the measurements. For example, EXAFS data of the Pt3 sample, as compared to Pt2, are noisier due to cell absorption and working conditions, so uncertainty values for this sample are obviously larger. In the present case, estimates of uncertainties affecting most structural parameters were carried out by looking at specific contour maps in parameter space.[22] In Fig. 10, two contour maps associated with the E_0-R_1 correlation (parameters highly correlated) obtained for Pt foil and Pt3 samples are shown. The value of the error bar associated with the structural parameter R_1 has been obtained by calculating the value of the projection of the inner ellipse major axis on the R_1 axis. The third- and

TABLE IV. Structural parameters of the three-body configurations obtained by GNXAS analysis for each sample, where σ^2_Θ (deg^2) is the variance, $\rho_{r,r'}$, $\rho_{r,\Theta}$ are dimensionless bond-bond and bond-angle correlation parameters, respectively, and f is a fixed value.

	Pt foil			Pt1			Pt2			Pt3		
Angle	σ^2_Θ	$\rho_{r,r'}$	$\rho_{r,\Theta}$	σ^2_Θ	$\rho_{r,r'}$	$\rho_{r,\Theta}$	σ^2_Θ	$\rho_{r,r'}$	$\rho_{r,\Theta}$	σ^2_Θ	$\rho_{r,r'}$	$\rho_{r,\Theta}$
120°_f	3.0(5)	−0.4(1)	0.08(5)	4.0(5)	−0.4(1)	0.12(5)	4(1)	−0.4(2)	0.0(1)	3(2)	−0.4(3)	0.0(2)
180°_f	6(1)	−0.07(2)	0.0_f	8(1)	−0.11(2)	0.0_f	18(8)	−0.2(1)	0.0_f	20(15)	−0.2(2)	0.0_f

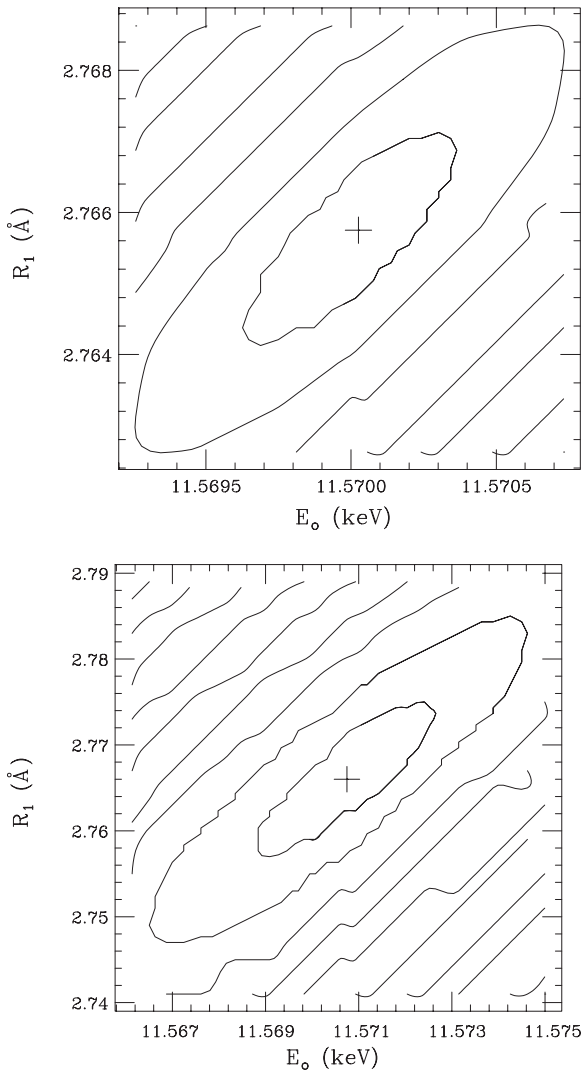

FIG. 10. Two-dimensional contour plots presenting E_0-R_1 correlations obtained for fitting the EXAFS spectra of (top) Pt foil and (bottom) Pt3 (the noisiest spectra). The inner elliptically shaped curves represent 95% confidence interval.

fourth-shell R and σ^2 parameters and their error bars were evaluated using their relationships with those defining the corresponding three-atom configurations (see Tables II and III and Refs. 22 and 33).

The overall quality of the spectra collected *in situ*, however, is very good with well-defined oscillations up to $k=18$ Å^{-1} at room temperature. We conclude that *in situ* EXAFS data (Pt3) can be safely analyzed, giving results compatible with parallel *ex situ* measurements (Pt2).

It is useful to discuss in detail and compare the results of the structural refinement of the nanocrystalline powders. Let us start looking at the decrease in coordination numbers and degeneracy of the three-body contribution observed in Pt1–Pt3 samples. The degeneracy values can be used to estimate the weighted mean particle size by using directly EXAFS data and the curves depicted in Fig. 6. For unsupported quasispherical Pt particles (Pt1), we obtain a mean particle size of 5.7 ± 1.0 nm, a result placed in the middle of those obtained by TEM and XRD (see Table I). The same result can be obtained using coordination numbers with mean interatomic distances and equation introduced for homogeneous spheres in Refs. 49 and 50. The spread of results about the Pt1 mean particle size obtained by different techniques can be possibly explained using the same arguments briefly explained in Sec. II B. Summarizing, XRD analysis generally overestimates the mean cluster size when even a limited fraction of larger particles is present in the sample.[14] In the Pt1 sample, the tail of the distribution includes grains of about 8–9 nm, as shown by TEM, and this can lead to an apparent shift of the mean size. At the same time, the presence of nanoparticle aggregates, observed in the Pt1 sample, disturbs the image-analysis process based on the selection and size measurement of individual particles. In this way, the weight of larger particles and, therefore, the final mean diameter could have been slightly underestimated due to the opacity of thicker sample regions. For Pt2 and Pt3 samples (supported Pt nanoparticles), coordination numbers and degeneracy determined by EXAFS were used to estimate mean diameters for both quasispherical and hemispherical cluster shapes (see Fig. 6). The mean diameter of Pt2 nanoparticles was found to be 2.3 and 3.0 nm for spherical and hemispherical models, respectively. Within the uncertainty estimated for particle size (±0.4 nm), both results are in good agreement with TEM and XRD data (see Table I). For the Pt3 sample, measured *in situ*, the cluster size was found to be 2.1 ± 0.3 and 2.8 ± 0.3 nm for quasispherical and hemispherical models, respectively. These values are in very good agreement with *ex situ* results (Pt2), showing the possibility of using nondestructive *in situ* EXAFS measurement to control time-dependent changes in nanogranular structure (e.g., agglomeration) occurring during potential cycling of the MEA.[51]

It is important to remark that this detailed and sophisticated structural analysis shows that EXAFS can be used to select between different models of cluster shape only for very small clusters (smaller than 2 nm), while uncertainty is still too high to determine the cluster atomic arrangement for particles of larger size as suggested in Ref. 4.

The presence of a significant fraction of "surface" ill-coordinated atoms with unbalanced bonds at the interface leads generally to a change in the first-neighbor (and farther shell) distribution, with marked increase in the bond variance, presence of an asymmetry, and a possible slight contraction of the average bond distance.[4,7,48,52] Therefore, we now discuss results about changes in the first-neighbor distribution as a function of particle size.

The bond disordering for nanocrystalline samples is evident when looking at variances (σ^2 in Tables III and IV) for what concerns both interatomic distances and angles. In general, we observe an increase in the σ^2 parameter upon decreasing the particle size (see results for Pt1 and Pt2). For Pt1 sample, the changes with respect to bulk Pt are similar to those reported in the literature.[3,4,52] However, disordering for Pt2 and Pt3 samples, particularly for the first-neighbor bond distribution, is somewhat higher than expected (about 50% increase for first-neighbor bond variance in Pt3). The first-neighbor bond variance is here determined with high accuracy, as it is used to compute most of the MS individual signals related to two-body and three-body configurations

including first neighbors. Moreover, the agreement between model and experimental signals is very good in an extended k range, so correlations among parameters are minimized. A broadening of size distribution[7] or/and interaction with support and with solubilized ionomer (like Nafion® polymer) used during the electrode and MEA preparation, and additionally, with water and fuel gas particles (case of the Pt3 sample, measured in fuel cell working conditions), may be reasonable explanations for the increase of static disorder, but this must be better explained by detailed *in situ* studies. The asymmetry parameter β is also found to increase in the nanocrystalline samples, as expected. Such an asymmetric first-neighbor distribution shifts the most probable value of the bond distance to shorter distances, with a tail more extended to large distances. This is likely to be the effect of the distribution of those surfacelike atoms, whose bonds are oriented only toward the inner atoms of the cluster. We believe that previous results mentioning a measurable contraction of the average bond distance in these systems can be understood in terms of a shortening of the most probable value of the distribution.

V. CONCLUSIONS

In this paper, we have presented detailed results of a MS EXAFS data analysis of crystalline and nanocrystalline platinum. Quantitative structural results have been obtained by using the GNXAS *ab initio* data-analysis method based on an expansion of the absorption cross section in terms of n-body MS contributions, here limited to include local two-body and three-body configurations up to the fifth neighbors. Best-fit simulations of the EXAFS spectra have been shown to give reliable information about local structure and dynamics of bulk Pt, and then various important parameters for MS EXAFS data analysis (muffin-tin potentials, mean free path, and atomic background) were also used for nanocrystalline Pt.

We have focused our work on Pt nanoparticles used as catalysts, aiming to establish a reliable framework for analyzing their structure *in situ*, under real operating conditions. With the purpose of a robust structural refinement of Pt nanoparticles, EXAFS data analysis has been used in combination with electron microscopy and x-ray diffraction, accounting for the actual size distribution and morphology.

EXAFS spectra of unsupported and supported Pt nanocrystalline systems have been analyzed, accounting for the reduction of the coordination number and degeneracy of triplet configurations, resulting from the measured size distribution. We have found that it is very important to account for the different reduction factors associated with first or distant shells or three-body configurations. Obtained EXAFS results have been found compatible with XRD and TEM results. We have shown that with the present methods and quality of the data, the possibility of selecting among different cluster shapes by using EXAFS data is limited to cluster sizes below 2 nm. We have also shown that EXAFS is able to provide a reliable measurement of the local distribution of distances and angles in these nanocrystalline systems. In particular, we have obtained that the first-neighbor distribution is broader and more asymmetric than in bulk Pt, and that local disorder increases upon reducing the dimensions of the particles.

In conclusion, the methodology presented in this paper has been found to be successful for a robust structural refinement of monatomic nanocrystalline systems and represents a solid starting point for analyzing subtle structural and dynamical local changes occurring during *in situ* experiments involving supported catalysts. It should be noted, however, that there are other important effects to be accounted for in analyzing the EXAFS spectra of nanocrystalline systems useful in applications, such as oxide layers and interaction or functionalization with components of the surrounding environment, which will need further development.

ACKNOWLEDGMENTS

We gratefully acknowledge the support of the BM29 staff at the European Synchrotron Radiation Facility (MA-121 proposal) and the Synchrotron Light Laboratory ELETTRA and beamline staff (XAFS 11.1 station). We would like to thank the Camerino former CIGA staff members (now Dip. di Fisica) M. Minicucci, L. Petetta, and G. Cantalupo for their invaluable help during the SEM, TEM, and XRD measurements. This research has been carried out within the NUME Project "Development of composite proton membranes and of innovative electrode configurations for polymer electrolyte fuel cells" (MIUR, FISR 2003).

*Present address: CNR-ISM Roma and Department of Physics, University of Camerino, I-62032 Camerino, Macerata, Italy; agnieszka@mif.pg.gda.pl

†Permanent address: CNISM, CNR-INFM CRS SOFT, Department of Physics, University of Camerino, I-62032 Camerino, Macerata, Italy.

[1] *X-Ray Absorption Fine Structure for Catalysts and Surfaces*, edited by Y. Iwasawa (World Scientific, Singapore, 1996), pp. 375–384.

[2] A. Di Cicco, M. Berrettoni, S. Stizza, E. Bonetti, and G. Cocco, Phys. Rev. B **50**, 12386 (1994).

[3] F. Boscherini, S. de Panfilis, and J. Weissmüller, Phys. Rev. B **57**, 3365 (1998).

[4] A. Frenkel, C. Hills, and R. Nuzzi, J. Phys. Chem. B **105**, 12689 (2001).

[5] J. H. Sinfelt, G. H. Via, and F. W. Lytle, J. Chem. Phys. **68**, 2009 (1978).

[6] A. Russell and A. Rose, Chem. Rev. (Washington, D.C.) **104**, 4613 (2004).

[7] A. Pinto, A. R. Pennisi, G. Faraci, G. D'Agostino, S. Mobilio, and F. Boscherini, Phys. Rev. B **51**, 5315 (1995).

[8] C. Lopez-Cartes, T. C. Rojas, R. Litran, D. Martinez-Martinez, J. M. de la Fuente, S. Penades, and A. Fernandez, J. Phys. Chem. B **109**, 8761 (2005).

[9] M. Dubiel, S. Brunsch, and L. Troger, J. Phys.: Condens. Matter **12**, 4775 (2000).
[10] A. Stakheev, O. Tkachenko, G. Kapustin, N. Telegina, G. Baeva, T. Brueva, K. Klementiev, W. Grunert, and L. Kustov, Russ. Chem. Bull. **53**, 528 (2004).
[11] G. Cheng, D. J. Carter, and T. Guo, Chem. Phys. Lett. **400**, 122 (2004).
[12] Y. Zhang, M. L. Toebes, A. van der Eerden, W. E. O'Grady, K. P. de Jong, and D. C. Koningsberger, J. Phys. Chem. B **108**, 18509 (2004).
[13] J. Ramallo-López, F. Requejo, A. Craievich, J. Wei, M. Avalos-Borja, and E. Iglesia, J. Mol. Catal. A: Chem. **228**, 299 (2005).
[14] S. Calvin, S. X. Luo, C. Caragianis-Broadbridge, J. K. McGuinness, E. Anderson, A. Lehman, K. H. Wee, S. A. Morrison, and L. K. Kurihara, Appl. Phys. Lett. **87**, 233102 (2005).
[15] A. I. Frenkel, S. Nemzer, I. Pister, L. Soussan, T. Harris, Y. Sun, and M. H. Rafailovich, J. Chem. Phys. **123**, 184701 (2005).
[16] R. Viswanathan, G. Hou, R. Liu, S. Bare, F. Modica, G. Mickelson, C. Segre, N. Leyarovska, and E. Smotkin, J. Phys. Chem. B **106**, 3458 (2002).
[17] C. Roth, N. Martz, T. Buhrmester, J. Scherer, and H. Fuess, Phys. Chem. Chem. Phys. **4**, 3555 (2002).
[18] R. Wiltshire, C. King, A. Rose, P. Wells, M. Hogarth, D. Thompsett, and A. E. Russell, Electrochim. Acta **50**, 5208 (2005).
[19] C. Roth, N. Benker, T. Buhrmester, M. Mazurek, M. Loster, H. Fuess, D. Koningsberger, and D. Ramaker, J. Am. Chem. Soc. **127**, 14607 (2005).
[20] E. Principi, A. Di Cicco, A. Witkowska, and R. Marassi, J. Synchrotron Radiat. **14**, 276 (2007).
[21] A. Filipponi, A. Di Cicco, and C. R. Natoli, Phys. Rev. B **52**, 15122 (1995).
[22] A. Filipponi and A. Di Cicco, Phys. Rev. B **52**, 15135 (1995).
[23] J. Langford, D. Louër, and P. Scardi, J. Appl. Crystallogr. **33**, 964 (2000).
[24] A. Di Cicco, R. Gunnella, R. Marassi, M. Minicucci, R. Natali, G. Pratesi, E. Principi, and S. Stizza, J. Non-Cryst. Solids **352**, 4155 (2006).
[25] P. Scherrer, Nachr. Ges. Wiss. Goettingen, Math.-Phys. Kl. **26**, 98 (1918).
[26] J. Langford and A. Wilson, J. Appl. Crystallogr. **11**, 102 (1978).
[27] G. Pratesi, A. D. Cicco, M. Minicucci, and J.-P. Itiè, J. Phys.: Condens. Matter **17**, 2625 (2005).
[28] A. Di Cicco, M. Minicucci, E. Principi, A. Witkowska, J. Rybicki, and R. Laskowski, J. Phys.: Condens. Matter **14**, 3365 (2002).
[29] E. A. Stern, R. W. Siegel, M. Newville, P. G. Sanders, and D. Haskel, Phys. Rev. Lett. **75**, 3874 (1995).
[30] E. A. Stern and K. Kim, Phys. Rev. B **23**, 3781 (1981).
[31] J. Goulon, C. Goulon Ginet, R. Cortes, and M. Dubois, J. Phys. (Paris) **43**, 539 (1982).
[32] L. Ottaviano, A. Filipponi, and A. Di Cicco, Phys. Rev. B **49**, 11749 (1994).
[33] A. Filipponi and A. Di Cicco, TASK Q. **4**, 575 (2000).
[34] G. Dalba, P. Fornasini, M. Grazioli, and F. Rocca, Phys. Rev. B **52**, 11034 (1995).
[35] A. Di Cicco and A. Filipponi, J. Non-Cryst. Solids **205-207**, 304 (1996).
[36] A. Di Cicco, M. J. Rosolen, R. Marassi, R. Tossici, A. Filipponi, and J. Rybicki, J. Phys.: Condens. Matter **8**, 10779 (1996).
[37] A. Di Cicco, M. Taglienti, M. Minicucci, and A. Filipponi, Phys. Rev. B **62**, 12001 (2000).
[38] E. Bus, J. Miller, A. Kropf, R. Prins, and J. A. van Bokhoven, Phys. Chem. Chem. Phys. **8**, 3248 (2006).
[39] A. Filipponi and A. Di Cicco, Phys. Rev. A **52**, 1072 (1995).
[40] A. Frenkel, J. Synchrotron Radiat. **6**, 293 (1999).
[41] S. I. Zabinsky, J. J. Rehr, A. Ankudinov, R. C. Albers, and M. J. Eller, Phys. Rev. B **52**, 2995 (1995).
[42] M. O. Krause and J. H. Oliver, J. Phys. Chem. Ref. Data **8**, 329 (1979).
[43] C. J. Powell and A. Jablonski, J. Phys. Chem. Ref. Data **28**, 19 (1999).
[44] A. Di Cicco and A. Filipponi, Phys. Rev. B **49**, 12564 (1994).
[45] G. van Dorssen, D. Koningsberger, and D. Ramaker, J. Phys.: Condens. Matter **14**, 13529 (2002).
[46] E. Groppo, C. Prestipino, C. Lamberti, P. Luches, C. Giovanardi, and F. Boscherini, J. Phys. Chem. B **107**, 4597 (2003).
[47] E. Sevillano, H. Meuth, and J. J. Rehr, Phys. Rev. B **20**, 4908 (1979).
[48] R. Benfield, A. Filipponi, N. Morgante, and G. Schmid, J. Organomet. Chem. **573**, 299 (1999).
[49] M. Borowski, J. Phys. IV **7**, C2 (1997).
[50] S. Calvin, C. J. Riedel, E. E. Carpenter, S. A. Morrison, R. M. Stroud, and V. G. Harris, Phys. Scr., T **T115**, 744 (2005).
[51] P. J. Ferreira, G. J. la O', Y. Shao-Horn, D. Morgan, R. Makharia, S. Kocha, and H. A. Gasteiger, J. Electrochem. Soc. **152**, A2256 (2005).
[52] R. Benfield, A. Filipponi, D. T. Bowron, R. J. Newport, S. J. Gurman, and G. Schmid, Physica B **208-209**, 671 (1995).